Time-Resolved Crystallographic Studies of the Heme Domain of the Oxygen Sensor FixL: Structural Dynamics of Ligand Rebinding and Their Relation to Signal Transduction[†,‡]

Jason Key,[§,||] Vukica Šrajer,[⊥] Reinhard Pahl,[⊥] and Keith Moffat*[,§,⊥,#]

Department of Biochemistry and Molecular Biology, University of Chicago, Chicago, Illinois 60637, Consortium for Advanced Radiation Sources, and Institute for Biophysical Dynamics, University of Chicago, Chicago, Illinois 60637

Received January 10, 2007; Revised Manuscript Received February 16, 2007

ABSTRACT: The FixL protein of *Bradyrhizobium japonicum* is a dimeric oxygen sensor responsible for initiating regulation of transcription of genes encoding proteins involved in nitrogen fixation and oxidative stress. It consists of an N-terminal heme-bound PAS domain, denoted *bj*FixLH, and a C-terminal histidine kinase domain whose enzymatic activity depends on the ligation state of the heme. To investigate the molecular basis for this dependence and the dynamics associated with conversion between ligated and unligated states, we have conducted time-resolved Laue diffraction studies of CO recombination in *bj*FixLH. Time-dependent difference Fourier maps from 1 μs to 10 ms after photolysis of the heme−CO bond show movement of the side chain of Leu236 and the H and I β-strands into the ligand binding pocket formerly occupied by CO. Long-range conformational changes are evident in the protein, driven by relaxation of steric interactions between the bound ligand and amino acid side chains and/or changes in heme stereochemistry. These structural changes fully reverse as CO rebinds to the heme. Spectroscopic measurements of CO recombination kinetics in *bj*FixLH crystals relate the behavior of crystalline *bj*FixLH to solution and provide a framework for our time-resolved crystallographic experiments. Analysis of the time-dependent difference Fourier maps by singular value decomposition reveals that only one significant singular value accounts for the data. Thus only two structural states are present, the photolyzed and the CO-bound states. The first left singular vector represents the difference in density between these two states and shows features common to difference maps calculated from the static CO and deoxy states. The first right singular vector represents the time course of this difference density and agrees well with the CO recombination kinetics measured spectroscopically. We refine the structure of the photolyzed state present in the early-microsecond time range and find that it does not differ significantly in conformation from static, deoxy *bj*FixLH. Thus, structural relaxation from CO-bound to deoxy *bj*FixLH is complete in less than 1 μs.

The Per-Arnt-Sim (PAS[1]) domain is a ubiquitous protein signaling module found in all kingdoms of life which allows organisms to sense and subsequently respond to environmental stimuli (*1*). This ∼100 amino acid domain is often expressed in tandem with an enzymatic domain whose activity is regulated by the PAS domain in response to an external stimulus (*2*−*5*). The roles of PAS proteins are diverse; some members bind prosthetic groups though others do not. As a class they show low sequence homology in spite of striking tertiary structural similarities (*6*). Among these proteins are photoreceptors (*7*), redox sensors (*8*), and small molecule sensors (*9*). Heme-PAS proteins form an important subgroup of PAS domain proteins which contain a covalently bound heme prosthetic group and exhibit catalytic control of their enzymatic domains in response to dissolved diatomic gases (*2*, *3*, *10*−*12*). Several heme-PAS proteins have been characterized including phosphodiesterase A1 of *Acetobacter xylinum* (*13*), the *Escherichia coli* protein DOS (*10*), the putative carbon monoxide sensor NPAS2 (*14*) from mice and humans, and the FixL proteins of nitrogen-fixing *Rhizobia* (*15*). Of these, the FixL proteins from the nitrogen-fixing bacteria *Bradyrhizobium japonicum* (*bj*FixL) and *Sinorhizobium meliloti* (*sm*FixL) have been the most widely studied (see ref *12* for review of heme-PAS proteins).

[†] This work is supported by NIH Grants GM036452 and RR07707 (BioCARS).

[‡] Coordinates and structure factors have been deposited in the Protein Data Bank under ID codes 2OWJ and 2OWH.

* To whom correspondence should be addressed: Department of Biochemistry and Molecular Biology, Gordon Center for Integrative Science, 929 East 57th Street, University of Chicago, Chicago, IL 60637. E-mail: moffat@cars.uchicago.edu. Phone: 773-702-2116. Fax: 773-702-0439.

[§] Department of Biochemistry and Molecular Biology, University of Chicago.

[||] Current address: Vrije Universiteit Amsterdam, 1081HV Amsterdam, The Netherlands.

[⊥] Consortium for Advanced Radiation Sources.

[#] Institute for Biophysical Dynamics, University of Chicago.

[1] Abbreviations: PAS, an acronym formed from the names of the eukaryotic proteins period (PER), aryl hydrocarbon receptor nuclear translocator (ARNT), and simple-minded (SIM); *bj*FixLH, the heme-PAS domain of the FixL protein from *Bradyrhizobium japonicum*; CW, continuous wavelength; *sm*FixLH, the heme-PAS domain of the FixL protein from *Sinorhizobium meliloti*; SVD, singular value decomposition; rms, root mean square.

10.1021/bi700043c CCC: $37.00
Published on Web 03/27/2007

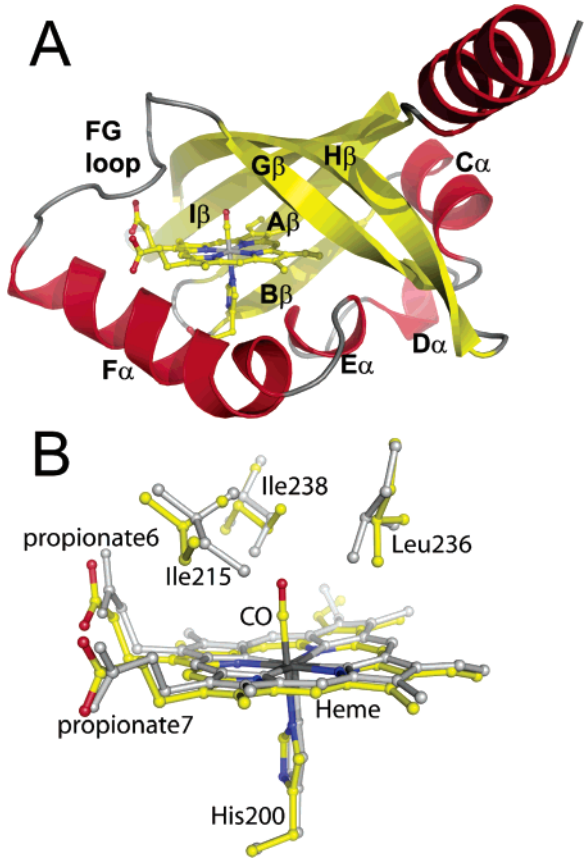

FIGURE 1: (A) Ribbon cartoon of the structure of *bj*FixLH in crystals in space group *R*32 (PDB code 1XJ2). Secondary structure elements are identified in their order in the primary structure (*17*). (B) A ball and stick rendition of the heme pocket of *bj*FixLH. The CO-bound conformation is shown in yellow, the deoxy state in gray.

*bj*FixL is a dimeric oxygen sensor responsible for initiating regulation of transcription of genes encoding proteins involved in nitrogen fixation and oxidative stress (*16*). Each monomer contains a single N-terminal heme-PAS sensory domain and a C-terminal kinase domain. The autophosphorylation activity of the histidine kinase is inhibited by ligand binding at the heme (*2*, *3*). The isolated heme-PAS domain of this protein, referred to as *bj*FixLH (Figure 1A), has been the subject of crystallographic studies which examine the mechanism of ligand recognition and signal transduction (*17*−*20*). In contrast to most globins, FixLs have a hydrophobic binding pocket and lack a distal histidine residue (Figure 1B). Upon binding of oxygen to deoxy *bj*FixLH, the heme alters its stereochemistry and the protein undergoes a conformational change both in the FG loop and in residues distal to the heme in the H and I β-strands of the core β sheet of the PAS domain. Rearrangement of the FG loop is accompanied by movement of Arg220 into the heme pocket where it forms an essential hydrogen bond with the bound oxygen (*18*, *19*). Carbon monoxide binding to FixL does not result in this FG loop switch, but similar structural changes are evident in the H and I β-strands. The FG loop in the CO-bound structure is only slightly shifted when compared to the O_2- and CN-bound structures (*21*); the side chain of Arg220 does not move into the pocket. These findings suggest that signaling upon ligand binding in *bj*FixLH is at least partially achieved through the H and I β-strands distal to the heme. This region of the PAS β-sheet has been implicated in signal transduction in several other PAS domains of diverse function (*22*−*28*).

Carbon monoxide has been used for several decades as a molecular probe of protein dynamics associated with conformational change in heme proteins (*29*−*32*). The CO−iron bond in CO-bound heme is photolabile and can be ruptured by light with high quantum efficiency. This makes it possible to rapidly generate a state of the protein that is far from equilibrium, to initiate the relaxation of structure toward the unliganded deoxy state, and to monitor rerelaxation to the CO-bound state as CO ultimately rebinds. Using time-resolved Laue X-ray crystallography (see ref *33*−*36* for reviews) it is possible to visualize changes in the positions of all atoms within a protein during such processes, thus revealing the structural dynamics of the entire protein as it performs its function. Time-resolved crystallography has been extensively applied to both wild type and mutant forms of the oxygen storage and transport protein myoglobin (*37*−*43*), to a dimeric hemoglobin which retains cooperative allosteric binding in its crystal lattice from the clam *Scapharca inaequivalvis* (*44*), and to the bacterial blue-light photoreceptor PYP (*23*, *45*, *46*). In addition, initial time-resolved studies have been carried out on the photosynthetic reaction center (*47*).

We present time-resolved X-ray diffraction studies of CO recombination in *bj*FixLH to reveal the nature of the structural changes and the time course by which they develop. By comparison with globins, little is known about the dynamics of CO recombination within the widely distributed heme-PAS domain, for which the bimolecular association rate constant for CO rebinding at ambient temperature is 100-fold lower than in wild-type sperm whale myoglobin (*10*). Time-resolved crystallographic datasets were collected using Laue diffraction at ambient temperature at 16 delay times from 1 μs to 10 ms after CO photolysis in order to directly visualize the photolyzed *bj*FixLH structure, rebinding of CO ligand, and relaxation of the heme and the protein. Singular value decomposition (SVD) analysis of the resulting 16 time-resolved difference Fourier maps identifies the number and nature of significant structural components (*46*, *48*, *49*). The application of time-resolved crystallography to *bj*FixLH is particularly challenging for two reasons: *bj*FixLH crystals exhibit relatively modest diffracting power, and the structural changes associated with protein relaxation and CO binding turn out to be small in spatial extent (*18*, *21*). However, substantial improvements in the time-resolved Laue method (*50*), data processing (*51*), noise reduction (*52*), and electron density visualization (*39*) allow us to successfully apply this technique to *bj*FixLH, whose crystals are of a moderate diffraction quality more typical of the majority of protein crystals than are those of myoglobin or PYP. In addition, we report transient absorbance flash-photolysis measurements of carbon monoxide rebinding in *bj*FixLH crystals and compare these with solution studies.

MATERIALS AND METHODS

Protein Purification and Crystal Preparation. *bj*FixLH protein was expressed and purified as described (*53*). The crystals were grown, converted to the CO state, and mounted in capillaries under CO as described (*21*). Rhombohedral crystals of *bj*FixLH in space group *R*32 were used for time-

resolved Laue diffraction due to their high symmetry and low mosaicity. The concentration of heme (and CO) in the crystals is 38 mM. Crystals were mounted 1−2 days prior to data collection, though no oxidation was observed spectroscopically over several weeks.

X-ray Data Collection. The rhombohedral *bj*FixLH crystals grow in a disk-like morphology and were mounted with the thin dimension facing the capillary wall in order to present the shortest dimension to the laser to achieve maximum photolysis. Crystals were photolyzed by a 7.5 ns (fwhm) laser pulse at 615 nm produced by a Nd:YAG pumped dye laser (Continuum) containing rhodamine 610/640 laser dye. The pulse was delivered to the crystal through either one or two optical fibers focused to a spot with ~1 mm diameter at the crystal. The total laser pulse energy was 1.5-2 mJ. A wavelength of 615 nm was used to penetrate the optically dense crystal on the red edge of the α peak of the CO−*bj*FixLH absorption spectrum. The optical density at this wavelength of a typical crystal was 0.25. Temperature was maintained at 14 °C at the crystal by a cooled gas stream to minimize the temperature rise arising from heat deposited by repeated laser flashes. Laue X-ray diffraction data were collected on a MarCCD 165 detector at the 14-ID-B station of BioCARS, at the Advanced Photon Source (APS), Argonne, IL. This beamline employs an APS Undulator A insertion device which was set at 25 mm gap. At this gap the first harmonic of the undulator lies at 1.085 Å wavelength. All experiments were conducted in pump−probe mode in which a laser pulse to initiate CO photolysis—the pump—was followed after an adjustable delay time by the X-ray pulse or pulse train—the probe. Delay times, defined by the time between the centers of the X-ray and laser pulses, ranged from 1 μs to 10 ms. Delay times from 1 to 7 μs used a 500 ns X-ray pulse train. For delay times of 10 μs or longer, a 2 μs X-ray pulse train was used to enhance the X-ray intensity and minimize the number of exposures. A typical Laue dataset consisted of 40 light (with laser flash) and 40 complementary dark Laue diffraction images spaced by 3° in angular setting of the crystal. Redundant datasets were collected at several delay times to allow averaging that maximized signal-to-noise and data completeness.

Data Reduction, Difference Fourier Maps, and Singular Value Decomposition Analysis. Laue diffraction data was processed using the *Precognition* Laue processing software package (*54*). All data were integrated to a resolution of 2.5 Å. Difference structure factor amplitudes for each time point, ΔF, were calculated by subtracting the dark structure factor amplitudes from the light. Difference structure factors were then weighted according to their magnitudes and standard deviations as described in Ursby et al. (*52*) and Šrajer et al. (*40*). Phases for each reflection were calculated using the static room-temperature structure of the CO−*bj*FixLH complex (PDB code 1XJ2) (*21*). Difference Fourier maps were calculated for each dataset from a single crystal in order to minimize systematic error associated with crystal to crystal variation. A single ΔF dataset at each delay time was produced by averaging redundant time points. The completeness and redundancy of all data is presented in Table 1, and statistics for the 16 difference datasets in Table 2. Restrained refinement of the CO-bound and photolyzed states of *bj*FixLH was carried out using datasets calculated from all data spanning delay times from 1 to 3 μs, using the program REFMAC5 from the CCP4 package (*55*). Refinement statistics are presented in Table 3. Estimation of the extent of photolysis and extrapolation of electron density to 100% photolysis were carried out as described by Schotte et al. (*39*). Briefly, maps are calculated from extrapolated structure factors according to the formula $F_{phot} = F_{dark} + (2/x)(F_{light} - F_{dark})$ where F_{dark} and F_{light} are the experimentally determined CO-bound and partially photolyzed structure factor amplitudes and F_{phot} represents structure factors of a 100% photolyzed state. The fractional extent of photolysis, x, is calculated from electron density maps by estimating the point at which CO density is no longer observable and density of the heme iron is fully extended from the porphyrin in extrapolated maps. Figures of difference Fourier maps were created using the programs *Ribbons* (*56*) and pymol (*57*). SVD of time-resolved difference Fourier maps was carried out with the program *SVD4TX* (*48*). SVD decomposes time-dependent data into its orthonormal time-independent components in the form of left singular vectors, or lSVs, and identifies the time course associated with each component in a corresponding right singular vector, or rSV (*48*, *49*, *58*). Light and dark maps, mapped nonlinearly to brightness in Figure 4, were created using equivalent reflections by Friedrich Schotte using the program *Lauemap* (*38*). Cavity analysis of *bj*FixLH was performed with VOIDOO (*59*).

CO Flash-Photolysis Kinetics in bjFixLH Crystals. CO flash photolysis optical measurements on crystals were carried out using a home-built microspectrophotometer (*60*). The pump laser pulse was provided as in the X-ray diffraction experiments. The change in absorption at 543 nm due to CO recombination after photolysis was measured using weak CW light from a He−Ne laser, where the change in light intensity transmitted by the crystals was recorded by a photomultiplier tube (Hamamatsu R955) and an oscilloscope (500 MHz Tektronix 744A). One thousand time-courses were collected and averaged to improve the signal-to-noise ratio.

RESULTS AND DISCUSSION

Evolution of Structural Change and Carbon Monoxide Rebinding within the Heme Pocket. The time-resolved crystallographic data series follows the evolution of structural change over 4 decades in time as CO rebinds after photolysis (Figure 2). All maps from the early delay times (1 to 3 μs) are very similar. The maps show the slow decay of a long-lived photolyzed state, characterized by a large negative feature on the CO, a highly displaced, domed porphyrin and heme iron, and the collapse of the distal hydrophobic residues, Leu236, Ile238, and Ile215 into the heme pocket after departure of the CO. Also evident are distinct difference features on the backbone atoms of the H and I β-strands at Leu236 and Val253 on the surface of the protein. Such features were previously identified in the refined structures of the CO and deoxy states in static CO − deoxy difference maps (*21*). Also notable are difference features on the side chain of the proximal histidine and the Fα-helix, on propionate 6 of the heme and on residues Pro212, His213, and Ile216 in the FG loop. This solvent-exposed region has exceptionally high temperature factors which are further elevated upon ligand binding (*21*). As a consequence, difference features in the FG loop and heme propionates are low in magnitude (from 2.8σ to 3σ, where σ is the rms value

Table 1: Time-resolved X-ray Data Statistics

time delay	crystal	R on (F^2) %	R on ($\|F\|$) %	no. of observations	no. of unique reflections	redundancy	completeness %	last shell % (2.59−2.50 Å)
1 μs	1	12.1	6.6	30069	5082	5.91	78.4	35.1
	2	12.6	6.9	33506	5372	6.24	82.8	43.3
	3	10.3	5.7	25912	5498	4.71	84.8	41.2
2 μs	3	12.2	6.5	25806	5470	4.72	84.3	41.2
	4	11.8	6.4	30271	5390	5.62	83.1	43.1
3 μs	1	11.4	6.4	30624	5088	6.02	78.5	39.3
	5	12.2	6.4	19689	5016	3.93	77.3	34.1
5 μs	6	14.1	7.5	18418	4872	3.78	75.1	36.3
	7	12.5	6.8	27969	5260	5.32	81.1	41.8
7 μs	8	12.0	6.6	23565	5071	4.65	78.2	35.5
10 μs	9	12.7	6.9	83592	5941	14.07	91.6	65.1
	8	12.1	6.6	23573	4927	4.78	76.0	34.4
	10	11.4	6.4	30023	5332	5.63	82.2	37.0
20 μs	10	11.4	6.4	28829	5312	5.43	81.9	38.1
	5	12.4	6.5	20566	5178	3.97	79.8	34.7
	9	13.1	6.7	26557	5013	5.30	77.3	29.7
50 μs	9	11.3	6.3	31810	5455	5.83	84.1	42.8
	11	11.2	6.2	30932	5583	5.54	86.1	45.1
100 μs	11	11.1	6.1	32578	5477	5.95	84.5	45.2
	12	13.9	7.4	26404	5065	5.21	78.4	35.5
	13	14.3	7.6	24433	5033	4.85	77.6	36.5
200 μs	14	13.1	7.1	28817	5325	5.41	82.1	38.9
300 μs	15	12.0	6.5	31745	5373	5.91	82.8	38.9
	16	10.3	5.7	19872	5131	3.87	79.1	37.6
500 μs	17	11.1	6.2	20014	5331	3.75	82.2	37.9
1 ms	18	12.7	7.0	43724	5314	8.23	82.0	48.6
2 ms	19	11.7	6.5	44792	5700	7.86	87.9	55.3
5 ms	20	12.2	6.6	48033	5826	8.24	89.8	59.6
10 ms	21	13.1	7.0	40915	5552	7.37	85.6	52.3
	20	12.9	6.9	42117	5826	7.23	89.8	59.6
				Reference (dark)				
	1	8.2	4.9	34669	5438	6.37	83.9	47.8
	2	11.1	6.1	40823	5724	7.13	88.3	49.1
	3	10.0	5.5	27591	5682	4.85	87.6	48.0
	4	8.7	5.0	34829	5743	6.06	88.6	50.1
	5	12.7	6.7	20711	5159	4.01	79.6	35.2
	6	10.6	5.7	27434	5606	4.89	86.4	45.2
	7	11.3	6.2	33855	5599	6.05	86.4	45.2
	8	12.0	6.4	26541	5343	4.97	82.4	39.9
	9	10.4	5.8	32883	5468	6.01	84.3	43.9
	10	10.3	5.9	31587	5503	5.74	84.9	42.3
	11	8.7	5.1	34466	5747	6.00	88.6	49.6
	12	12.3	6.7	20711	5464	3.79	84.3	41.8
	13	11.5	6.2	32231	5600	5.76	86.4	48.1
	14	11.4	6.3	33355	5684	5.87	87.6	49.3
	15	11.5	6.3	44334	5656	7.84	87.2	47.8
	16	8.6	4.7	20486	5118	4.00	78.9	36.5
	17	11.1	6.2	21039	5516	3.81	85.1	41.4
	18	12.8	7.0	45730	5350	8.55	82.5	49.6
	19	12.2	6.6	57112	5758	9.92	88.8	55.9
	20	12.1	6.5	49880	5905	8.45	91.1	61.1
	21	12.0	6.5	45776	5700	8.03	87.9	53.2

of the difference electron density across the asymmetric unit). The photolyzed state persists relatively unchanged in structure from 1 μs to 100 μs. From 100 to 300 μs, the first signs of ligand rebinding are evident through a decrease in magnitude of the features associated with the CO, the heme iron, and the backbone atoms of the distal β-sheet residues. From 300 μs to 1 ms, substantial CO rebinding takes place, evidenced by rapid decay of most distal side chain features, followed by loss of the features originating from the movement of the side chain of Leu236. Only a trace of the large negative CO feature remains at 5 ms, by which time the CO has nearly fully rebound. The 10 ms difference map is featureless and displays only noise: CO rebinding and structural relaxation to the reactant (the CO-bound state) is complete.

Structural Changes in the bjFixL PAS Domain. In order to reveal the smaller global conformational changes that occur in the protein following photolysis, electron density maps were constructed from the time-resolved diffraction data using the visualization technique of Schotte et al. (*39*). This approach allows a different presentation of data to better visualize subtle structural changes by mapping electron density nonlinearly to color brightness. Structural changes are presented as a color gradient across atoms that move, while nonlinear mapping of density highlights weak features. These maps, a superposition of the F_o^{light} and F_o^{dark} Fourier maps instead of ΔF difference maps, reveal structural relaxation throughout *bj*FixLH upon photolysis (Figure 3).

The steric interaction between CO and the distal side chains flanking the ligand pocket and the change in stereo-

Table 2: Averaged Difference Datasets[a]

time delay	no. of unique reflections	overall completeness %	completeness last shell % (2.59 − 2.50 Å)
1 μs	6037	93.1	60.4
2 μs	5784	89.2	46.5
3 μs	6005	92.6	56.5
5 μs	5556	85.7	42.8
7 μs	5071	78.2	35.5
10 μs	5964	92.0	53.5
20 μs	5899	91.0	49.8
50 μs	5957	91.9	53.6
100 μs	5943	91.6	53.2
200 μs	5318	82.0	33.0
300 μs	6017	92.8	60.3
500 μs	5327	82.1	37.6
1 ms	5313	82.0	31.0
2 ms	5319	82.0	37.6
5 ms	5570	85.9	48.1
10 ms	5790	89.3	54.6

[a] Difference structure factor amplitudes were calculated from light and dark data collected from the same crystals to 2.5 Å resolution and then averaged over multiple datasets collected at the same time delay.

Table 3: Refinement Statistics for Dark and Photolyzed *bj*FixLH Time-Resolved Laue Data

	dark CO− *bj*FixLH	photolyzed *bj*FixLH, extrapolated to 100% photolysis
completeness to 2.5 Å (%) (last shell, 2.59−2.50 Å)	97.4 (84.3)	97.4 (84.3)
unique reflections	6352	6352
R_{work}, R_{free} (%)[a]	21.3, 29.1	23.8, 30.1
rmsd from ideal bond lengths (Å)	0.016	0.023
rmsd from ideal bond angles (deg)	1.608	2.433

[a] $R_{work} = \sum|F_{obs} - F_{calc}|/\sum|F_{obs}|$, where F_{obs} and F_{calc} are the observed and calculated structure factors, respectively. R_{free} is calculated from a randomly selected subset of the data (5%) excluded from refinement.

chemistry of the heme are the two main factors that initiate protein relaxation after photolysis. Relaxation of protein structural elements can be primarily associated with either factor or with their combination. The movement of the distal β-sheet is driven by steric interactions with the ligand. Movement of the distal side chains of β-sheet residues into the pocket necessitates movement of backbone atoms and produces a longer-range conformational change. As noted in difference maps described above (Figure 2), the side chains of Leu236 and Leu238 move into the hole vacated by the newly photolyzed CO. The main chain atoms of these residues also move, as do the other residues in the distal β-sheet to which their main chains are hydrogen-bonded. Changes in the distal β-sheet of the molecule extend over the face of the sheet and are most prominent in residues of the I β-strand at residue Arg254, more than 15 Å distant from the location of the bound CO. A lateral movement of the heme is also evident, a consequence of the relaxation of steric hindrance between the CO-liganded heme and the side chain of Leu236. This movement shifts the heme away from the FG loop toward the interior of the PAS domain and is also evident in the coupled movement of His200 and the side chain of Phe176. The steric interaction between the heme and Phe176 displaces the Cα helix to which Phe176 belongs. Ultimately, this helix and both the CD and GH loops are shifted outward from the core of the domain. On the proximal side of the heme, structural changes in His200 and the Fα helix are driven by heme doming and the movement of the heme iron out of the porphyrin plane upon spin state change. Heme doming is indicated by positive and negative difference electron density features flanking the heme plane. The main chain atoms of the Fα helix are displaced away from the heme, while the side chains of Tyr203 and Met192 move toward the heme to fill space created by upward movement at the porphyrin periphery. Finally, the FG loop moves in response to both factors: the doming and lateral movement of the heme propionate groups along with the steric interaction between Ile215 with ligand. The central portion of the FG loop, from residues His213 to Ile215, moves toward the heme pocket after photolysis, while residues Ile216 to Ile218 move away from the heme pocket, driven upward by the movement of the propionates as the heme changes from a planar to a domed conformation. Conformational differences are evident in the water molecules coordinated to the FG loop at the side chains of residues His213 and Arg206. Thus, conformational relaxation upon CO photolysis involves structural changes at considerable distance from the site of ligand binding in several regions of the protein.

Optical Studies of CO Recombination in bjFixLH Crystals. We examined CO recombination spectroscopically in crystals of *bj*FixLH to characterize CO recombination in crystals, to relate this to known solution behavior, and to provide a framework for interpreting our crystallographic experiments. CO can indeed be efficiently photolyzed in crystals of *bj*FixLH at moderate laser energy per pulse ($\sim$1.25−2.5 mJ/mm^2). This was of concern because studies of myoglobin suggest that its crystals are considerably more difficult to photolyze than solution and there is a risk of causing irreversible damage to the crystals (*61*). Transient absorbance spectra show the rebinding of CO after photolysis of the *R*32 crystal form (Figure 4A). Also shown is a fit to an expression describing bimolecular CO rebinding where the ligand and the protein are equal in concentration, $C/(1 + kt)$, under the conditions which hold in the crystal where the concentrations of photolyzed *bj*FixLH and free CO are equal. A purely bimolecular scheme is appropriate since, despite significant unimolecular, geminate recombination for O_2 and NO in *bj*FixLH, no geminate recombination of CO has been observed (*62*, *63*). In the expression noted above, the rate k represents $k_{CO}[CO]_{phot}$, where k_{CO} is the second-order rate coefficient and $[CO]_{phot}$ is the concentration of CO molecules, initially bound to heme, that escape into the solvent following photolysis. The value for k derived from the fit is 7.35×10^2 s^{-1}. A value for $[CO]_{phot}$ of 19 mM is derived from the extrapolated electron density of the photolyzed state (discussed in detail below), which indicates that $\sim$50% of all CO molecules in the crystal yield a photolyzed CO to the solvent. Hence the value for k_{CO} is 3.9×10^4 M^{-1} s^{-1}, in a very good agreement with the second-order rate coefficient of 5×10^4 M^{-1} s^{-1} measured in solution (*53*). This suggests that the effects of crystallization mother liquor and the intermolecular forces in the crystal lattice on CO recombination are small. An even better mathematical fit to our spectroscopic data is achieved by a stretched exponential expression of the form $C \exp[(-kt)^{\beta}]$ (*64*). Such an expression introduces an additional parameter β. We do not feel that this more complex fit is justified in the light of the

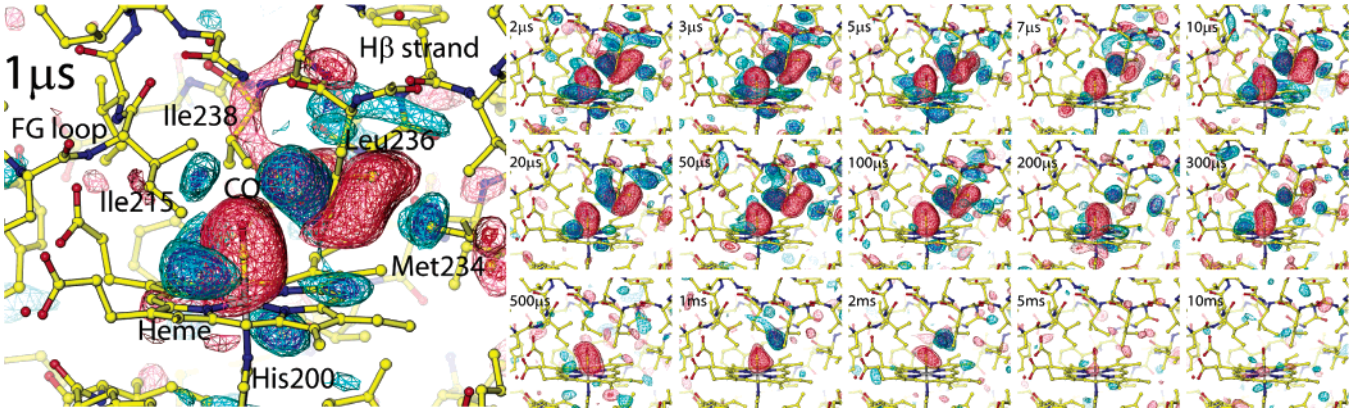

FIGURE 2: Sixteen time-resolved difference electron density maps from 1 μs to 10 ms after photolysis. Maps are contoured at $\pm 3.5\sigma$ and 4.5σ where blue is positive and red is negative, and σ is the root-mean-square value of the difference density across the asymmetric unit.

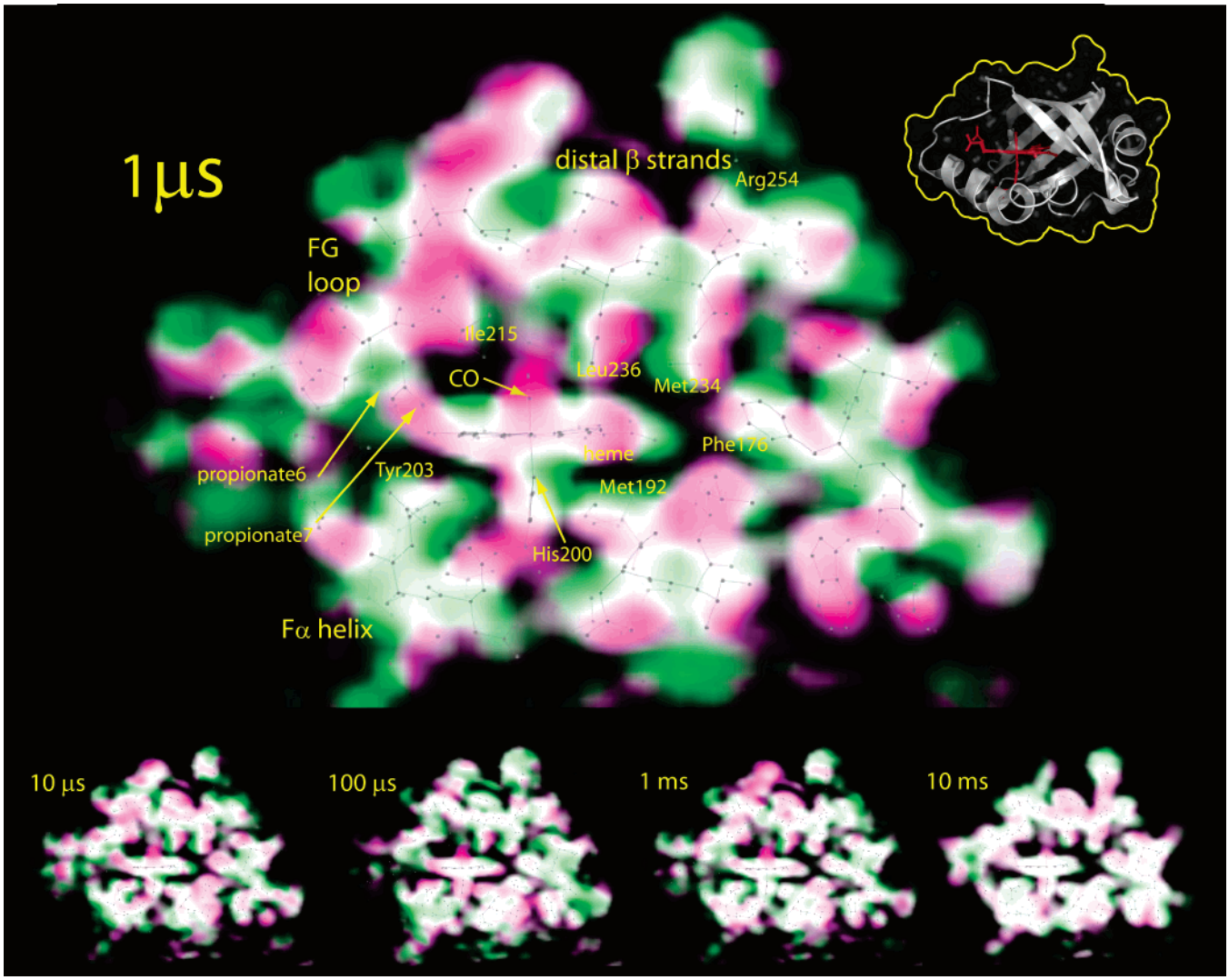

FIGURE 3: A superposition of time-dependent F_o^{light} and corresponding F_o^{dark} electron density maps. Shown are maps for the CO-bound ground state (magenta) and corresponding photolyzed state (green) at time delays from 1 μs to 10 ms. Maps are mapped nonlinearly to color brightness. The overlap of magenta and green in this superposition presentation of maps blends to white. The magenta-to-green color gradient indicates the direction of motion of protein atoms. The orientation is shown in the upper right corner as a ribbon model of the molecule in gray, with van der Waals surface outlined in yellow.

modest signal-to-noise of our data and the absence of a compelling physical model for stretched exponential behavior.

SVD Analysis of Time-Resolved Electron Density. In order to relate our time-dependent optical and crystallographic results, we performed SVD on the *bj*FixLH difference electron density maps (Figure 2). Application of SVD to our time-dependent difference electron density reveals one and only one significant singular value that accounts for all difference signals in the data. Thus only two states are

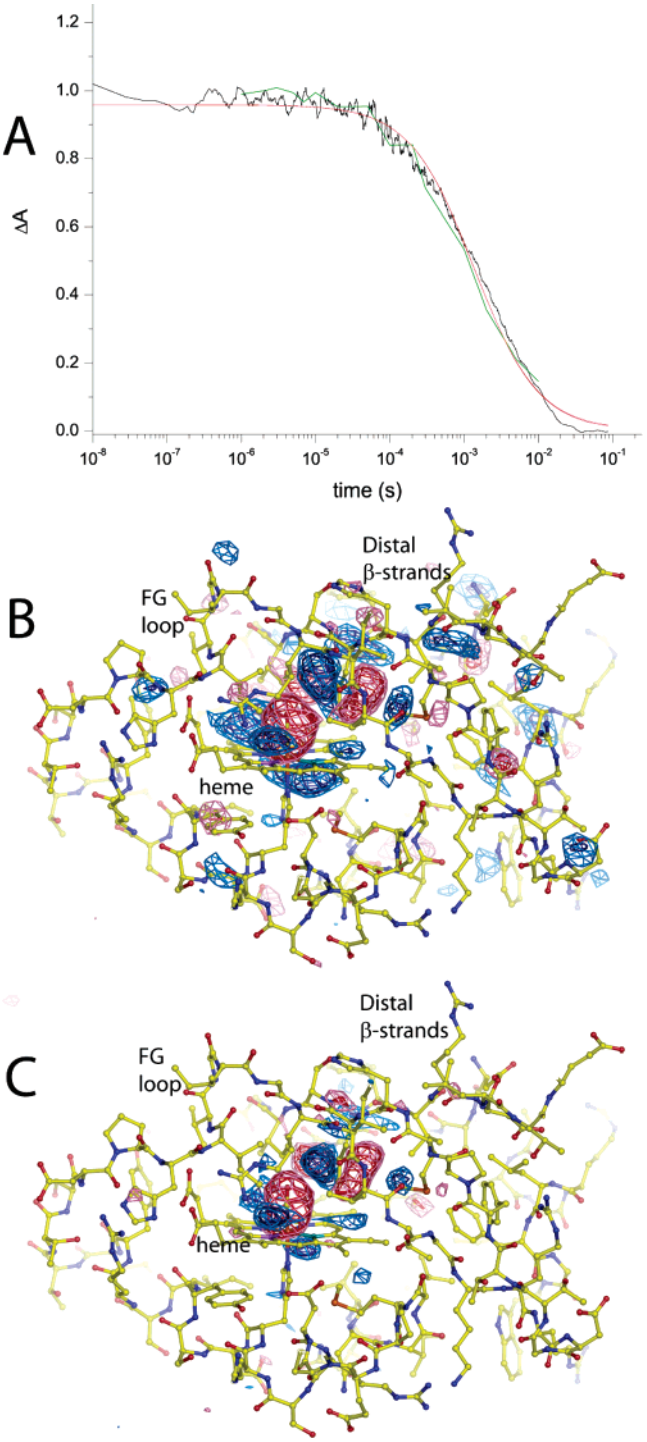

FIGURE 4: (A) CO recombination kinetics in *bj*FixLH crystals in space group *R*32, derived from transient absorbance change (black trace), a fit to a bimolecular expression (red), and the first right singular vector rSV1 derived from SVD analysis of time-resolved difference electron density (green). (B) The corresponding difference electron density lSV1 from SVD analysis, contoured at $\pm 3.5\sigma$ and $\pm 4.5\sigma$ where blue is positive and red is negative density. (C) The difference map created by averaging difference structure factors from all delay times from 1 to 3 μs.

present, namely, the CO-bound reactant and the product, photolyzed state (Figure 4B). The time-resolved data in the case of *bj*FixLH do not reveal any new, short-lived intermediate structures, in marked contrast with PYP (*23*, *46*). The time course of the decay of the lSV1 component of the data, namely, rSV1, agrees to within experimental error with the time course of CO rebinding measured optically (Figure 4A, green line). Evidently the optical and structural data are monitoring closely related recombination processes.

Because the SVD analysis indicates that only two structural states exist in our time-resolved difference maps, the early time points of the time-resolved data prior to substantial CO recombination represent this state most clearly. In order to assess the effect of the SVD analysis, the lSV1 difference map was compared with the averaged map derived from the ΔFs obtained from the 1 to 3 μs delay times (Figures 4B and C). As expected, the two maps are very similar and show the same principal structural features. The map derived from SVD (Figure 4B), however, has substantially better signal-to-noise ratio since the total noise is distributed among the remaining 15 left singular vectors. For example, the weak features associated with movement of the heme propionate 6, the FG loop, and the proximal side of the heme are greatly enhanced in the lSV1 map, as are long-range structural changes associated with the movement of the Hβ and Iβ-sheets of the protein at residue Arg254. Thus the difference map derived from SVD best represents the structure of the photolyzed state of *bj*FixLH 1 μs after photolysis of CO.

S*tructural Relaxation of bjFixLH to the Deoxy State.* In order to confirm whether complete structural relaxation of *bj*FixLH to the deoxy state occurs upon photolysis of the CO, as indicated by our SVD analysis, we compared the time-independent difference maps derived from SVD with a difference map calculated from experimental structure factor amplitudes obtained from static CO-bound and deoxy *bj*FixLH crystals (*21*). We also compared the coordinates of the photolyzed state obtained by refinement of the time-resolved Laue data with coordinates of the authentic deoxy state obtained by refinement of static crystallographic data (Figure 5, panels C, D, and F). Equivalent global conformational differences are evident in both the difference maps and the refined coordinates. In the electron density difference maps (Figure 5, panels A and B), structural change is evident from the heme to the distal β-strands. Difference electron density is present at lower levels in the experimental time-resolved maps than in calculated static electron density difference map due to the noise in the former. The noise present in the experimental maps, coupled with elevated temperature factors for the photolyzed state, gives rise to some apparent differences between the maps. These differences are associated with regions of the structure with exceptionally high *B*-factors. Temperature factor differences of greater than 20% have been noted between the liganded and unliganded forms of *bj*FixLH, specifically in the FG loop (*21*). A prominent difference between the maps which can be attributed to this effect can be seen at the side chain of Ile215 in the heme pocket. Common features are evident on the main chain atoms of Arg246 and in the FG loop of the molecule, however. These are the conformational changes most distant from the heme noted earlier (*21*), which suggests that propagation of structural changes in photolyzed *bj*FixLH is complete. Differences between refined coordinates of the CO-bound and photolyzed species show very similar changes in the distal β-strands and FG loop. The static CO and deoxy structures on the one hand, and time-resolved dark and photolyzed structures on the other, show the same conformational differences (Figure 5C and 5D). Furthermore, there are no major differences between either the static deoxy

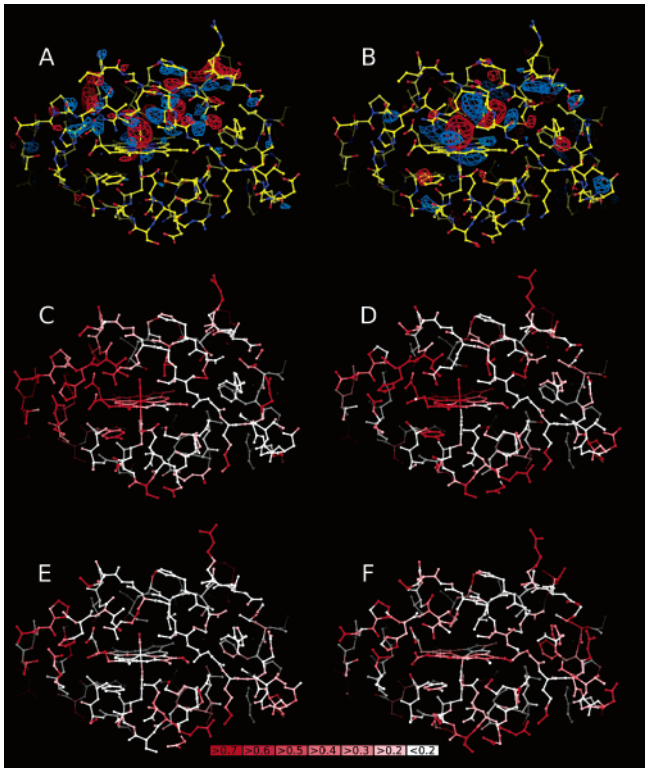

FIGURE 5: (A) F_c(deoxy) − F_c(CO) experimental electron density difference maps calculated from static structure factor amplitudes reported in ref *21*. (B) Electron density difference map *F*(photoproduct) − *F*(CO) derived from SVD of time-resolved electron density difference maps (lSV1). (C) CO−*bj*FixLH (from static measurements, PDB code 1XJ2) colored by difference in atomic position relative to static deoxy-*bj*FixLH (PDB code 1XJ3). Increasing red color corresponds increasing distance between refined coordinates (see key at bottom of figure, distance in angstroms). (D) CO−*bj*FixLH refined from "dark" Laue data (without laser flash) colored by difference in atomic position relative to refined photolyzed-*bj*FixLH coordinates. (E) CO−*bj*FixLH coordinates from "dark" Laue data colored by difference in atomic position relative to static CO−*bj*FixLH, PDB code 1XJ2. (F) Photolyzed-*bj*FixLH colored by difference in atomic position relative to deoxy-*bj*FixLH.

structure and the refined photoproduct state, or the static CO-bound and its time-resolved counterpart (Figure 5E and 5F). In all cases differences are confined to surface side chains of residues with high temperature factors. Thus, in both difference electron density maps and refined coordinates of the photoproduct, key conformational changes between the deoxy and CO structures are represented. This confirms that *bj*FixLH completely relaxes to a conformation identical to the static deoxy state within 1 μs after photolysis.

A Comparison with Myoglobin. Time-resolved crystallographic studies of the oxygen storage protein myoglobin have shown that relaxation to the deoxy state takes place over a large time range, with structural events taking place from picoseconds to milliseconds (*37*−*43*). This transition occurs on a rugged energy landscape populated by interconverting conformational substates (see ref *65* for review). This complexity gives rise to stretched exponential kinetics. *bj*FixLH has a significantly different protein fold and ligand binding properties than myoglobin, making its structural dynamics of interest. Our results show that structural relaxation from the CO-bound to the deoxy form of *bj*FixLH is rapid and is complete within 1 μs, despite the fact that overall CO recombination in *bj*FixLH is approximately 100-fold slower than sperm whale myoglobin (*10*). By comparison with myoglobin the energy landscape of CO-recombination in wild type *bj*FixLH appears relatively flat as assessed by ultrafast UV/visible spectroscopic techniques (*62*, *63*), but becomes more complex upon addition of the distal coordinating residue found in most globins (*66*). However, recent femtosecond infrared measurements suggest that CO recombination in *bj*FixLH is more complex on faster time scales (van Wilderen, Key, et al., in preparation). Time-resolved crystallography at delay times shorter than 1 μs is necessary to visualize if multiple structural processes occur following photolysis, or to confirm the apparent simplicity of this gas-modulated conformational switch.

In myoglobin, CO release from the protein matrix is characterized by a network of docking sites within the protein that are transiently occupied by outgoing CO. Sites have been found in myoglobin using static (*67*−*71*) and time-resolved techniques (*37*, *38*, *40*, *41*). For example, the half-life of the CO docked at the proximal (Xe1) docking site is ∼10 μs (see Figure 11 of ref *29*). A transiently docked CO molecule in *bj*FixLH with a similar half-life and peak occupancy would be detectable in our experiment. We therefore examined difference maps from 1 to 10 μs after photolysis to identify comparable CO docking sites in *bj*FixLH, in which CO would appear as a positive electron density difference peak. However, we could not positively identify any, despite the presence of a small hydrophobic cavity adjacent to the heme, bordered by the side chains of Phe176, Met234, and Val253 (not shown). Unlike myoglobin for which several cavities exist, this is the only cavity we detected in *bj*FixLH, and it might be too small (2.1 Å^3) to transiently accommodate an outgoing CO molecule. Further experiments using xenon binding (*67*) or cryotrapping (*68*, *69*) may be necessary to determine if other cavities exist in *bj*FixLH in crystals.

Implications for Signal Transduction. Prior studies of *bj*FixLH have suggested an ensemble ligand detection mechanism in which the structural signaling mechanism is not restricted to a single region of the protein and displays semiredundant aspects (*21*). Structural changes noted in the FG loop and in the β-sheet distal to the heme are coupled to the movement of the main chain atoms of Leu236 in the I strand, which allows the FG loop, the distal coordinating residue for O_2 (Arg220), and the β-sheet residues to act as a group. We observe significant difference density near Leu236 after exit of photolyzed ligand from the protein, and the associated shift of the residues of the H and I β-strands. Conformational changes are apparent at propionate 6 and in the FG loop residues Ile215 to Ile218. Thus the conformational elements of this ensemble sensing mechanism are present in our time-resolved difference maps: doming of the heme and subsequent propionate 6 movement and ligand shape sensed by steric clash of Leu236 with the bound ligand. Though additional support for an ensemble mechanism of this type has recently been reported (*65*), the means by which these structural changes inhibit kinase activity remains unclear.

ACKNOWLEDGMENT

J.K. thanks Sudarshan Rajagopal and Marius Schmidt for assistance with SVD analysis, and Friedrich Schotte and

Philip Anfinrud for preparation of brightness-mapped electron density maps.

REFERENCES

1. Taylor, B. L., and Zhulin, I. B. (1999) PAS domains: internal sensors of oxygen, redox potential, and light, *Microbiol. Mol. Biol. Rev. 63*, 479−506.
2. Gilles-Gonzalez, M. A., Gonzalez, G., and Perutz, M. F. (1995) Kinase activity of oxygen sensor FixL depends on the spin state of its heme iron, *Biochemistry 34*, 232−236.
3. Tuckerman, J. R., Gonzalez, G., Dioum, E. M., and Gilles-Gonzalez, M. A. (2002) Ligand and oxidation-state specific regulation of the heme-based oxygen sensor FixL from Sinorhizobium meliloti, *Biochemistry 41*, 6170−6177.
4. Hill, S., Austin, S., Eydmann, T., Jones, T., and Dixon, R. (1996) Azotobacter vinelandii NIFL is a flavoprotein that modulates transcriptional activation of nitrogen-fixation genes via a redox-sensitive switch, *Proc. Natl. Acad. Sci. U.S.A. 93*, 2143−2148.
5. Christie, J. M., Salomon, M., Nozue, K., Wada, M., and Briggs, W. R. (1999) LOV (light, oxygen, or voltage) domains of the blue-light photoreceptor phototropin (nph1): binding sites for the chromophore flavin mononucleotide, *Proc. Natl. Acad. Sci. U.S.A. 96*, 8779−8783.
6. Hefti, M. H., Francoijs, K. J., de Vries, S. C., Dixon, R., and Vervoort, J. (2004) The PAS fold. A redefinition of the PAS domain based upon structural prediction, *Eur. J. Biochem. 271*, 1198−1208.
7. Crosson, S., Rajagopal, S., and Moffat, K. (2003) The LOV domain family: photoresponsive signaling modules coupled to diverse output domains, *Biochemistry 42*, 2−10.
8. Martinez-Argudo, I., Little, R., Shearer, N., Johnson, P., and Dixon, R. (2004) The NifL-NifA System: a multidomain transcriptional regulatory complex that integrates environmental signals, *J. Bacteriol. 186*, 601−610.
9. Da Silva Xavier, G., Rutter, J., and Rutter, G. A. (2004) Involvement of Per-Arnt-Sim (PAS) kinase in the stimulation of preproinsulin and pancreatic duodenum homeobox 1 gene expression by glucose, *Proc. Natl. Acad. Sci. U.S.A. 101*, 8319−8324.
10. Delgado-Nixon, V. M., Gonzalez, G., and Gilles-Gonzalez, M. A. (2000) Dos, a heme-binding PAS protein from Escherichia coli, is a direct oxygen sensor, *Biochemistry 39*, 2685−2691.
11. Hofer, T., Spielmann, P., Stengel, P., Stier, B., Katschinski, D. M., Desbaillets, I., Gassmann, M., and Wenger, R. H. (2001) Mammalian PASKIN, a PAS-serine/threonine kinase related to bacterial oxygen sensors, *Biochem. Biophys. Res. Commun. 288*, 757−764.
12. Gilles-Gonzalez, M. A., and Gonzalez, G. (2005) Heme-based sensors: defining characteristics, recent developments, and regulatory hypotheses, *J. Inorg. Biochem. 99*, 1−22.
13. Chang, A. L., Tuckerman, J. R., Gonzalez, G., Mayer, R., Weinhouse, H., Volman, G., Amikam, D., Benziman, M., and Gilles-Gonzalez, M. A. (2001) Phosphodiesterase A1, a regulator of cellulose synthesis in Acetobacter xylinum, is a heme-based sensor, *Biochemistry 40*, 3420−3426.
14. Dioum, E. M., Rutter, J., Tuckerman, J. R., Gonzalez, G., Gilles-Gonzalez, M. A., and McKnight, S. L. (2002) NPAS2: a gas-responsive transcription factor, *Science 298*, 2385−2387.
15. Gilles-Gonzalez, M. A., Ditta, G. S., and Helinski, D. R. (1991) A haemoprotein with kinase activity encoded by the oxygen sensor of Rhizobium meliloti, *Nature 350*, 170−172.
16. Sciotti, M. A., Chanfon, A., Hennecke, H., and Fischer, H. M. (2003) Disparate oxygen responsiveness of two regulatory cascades that control expression of symbiotic genes in Bradyrhizobium japonicum, *J. Bacteriol. 185*, 5639−5642.
17. Gong, W., Hao, B., Mansy, S. S., Gonzalez, G., Gilles-Gonzalez, M. A., and Chan, M. K. (1998) Structure of a biological oxygen sensor: a new mechanism for heme-driven signal transduction, *Proc. Natl. Acad. Sci. U.S.A. 95*, 15177−15182.
18. Gong, W., Hao, B., and Chan, M. K. (2000) New mechanistic insights from structural studies of the oxygen-sensing domain of Bradyrhizobium japonicum FixL, *Biochemistry 39*, 3955−3962.
19. Hao, B., Isaza, C., Arndt, J., Soltis, M., and Chan, M. K. (2002) Structure-based mechanism of O2 sensing and ligand discrimination by the FixL heme domain of Bradyrhizobium japonicum, *Biochemistry 41*, 12952−12958.
20. Dunham, C. M., Dioum, E. M., Tuckerman, J. R., Gonzalez, G., Scott, W. G., and Gilles-Gonzalez, M. A. (2003) A distal arginine in oxygen-sensing heme-PAS domains is essential to ligand binding, signal transduction, and structure, *Biochemistry 42*, 7701−7708.
21. Key, J., and Moffat, K. (2005) Crystal structures of deoxy and CO-bound bjFixLH reveal details of ligand recognition and signaling, *Biochemistry 44*, 4627−4635.
22. Harper, S. M., Neil, L. C., and Gardner, K. H. (2003) Structural basis of a phototropin light switch, *Science 301*, 1541−1544.
23. Anderson, S., Šrajer, V., Pahl, R., Rajagopal, S., Schotte, F., Anfinrud, P., Wulff, M., and Moffat, K. (2004) Chromophore conformation and the evolution of tertiary structural changes in photoactive yellow protein, *Structure 12*, 1039−1045.
24. Erbel, P. J., Card, P. B., Karakuzu, O., Bruick, R. K., and Gardner, K. H. (2003) Structural basis for PAS domain heterodimerization in the basic helix−loop−helix-PAS transcription factor hypoxia-inducible factor, *Proc. Natl. Acad. Sci. U.S.A. 100*, 15504−15509.
25. Chen, J., Zou, A., Splawski, I., Keating, M. T., and Sanguinetti, M. C. (1999) Long QT syndrome-associated mutations in the Per-Arnt-Sim (PAS) domain of HERG potassium channels accelerate channel deactivation, *J. Biol. Chem. 274*, 10113−10118.
26. Morais Cabral, J. H., Lee, A., Cohen, S. L., Chait, B. T., Li, M., and Mackinnon, R. (1998) Crystal structure and functional analysis of the HERG potassium channel N terminus: a eukaryotic PAS domain, *Cell 95*, 649−655.
27. Kurokawa, H., Lee, D. S., Watanabe, M., Sagami, I., Mikami, B., Raman, C. S., and Shimizu, T. (2004) A redox-controlled molecular switch revealed by the crystal structure of a bacterial heme PAS sensor, *J. Biol. Chem.* 279 20186−20193.
28. Park, H., Suquet, C., Satterlee, J. D., and Kang, C. (2004) Insights into signal transduction involving PAS domain oxygen-sensing heme proteins from the X-ray crystal structure of Escherichia coli Dos heme domain (Ec DosH), *Biochemistry 43*, 2738−2746.
29. Anfinrud, P. A., Han, C., and Hochstrasser, R. M. (1989) Direct observations of ligand dynamics in hemoglobin by subpicosecond infrared spectroscopy, *Proc. Natl. Acad. Sci. U.S.A. 86*, 8387−8391.
30. Austin, R. H., Beeson, K. W., Eisenstein, L., Frauenfelder, H., and Gunsalus, I. C. (1975) Dynamics of ligand binding to myoglobin, *Biochemistry 14*, 5355−5373.
31. Lim, M., Jackson, T. A., and Anfinrud, P. A. (1993) Nonexponential protein relaxation: dynamics of conformational change in myoglobin, *Proc. Natl. Acad. Sci. U.S.A. 90*, 5801−5804.
32. Scott, E. E., and Gibson, Q. H. (1997) Ligand migration in sperm whale myoglobin, *Biochemistry 36*, 11909−11917.
33. Bourgeois, D., and Royant, A. (2005) Advances in kinetic protein crystallography, *Curr. Opin. Struct. Biol. 15*, 538−547.
34. Moffat, K. (1998) Ultrafast time-resolved crystallography, *Nat. Struct. Biol. 5*, 641−643.
35. Moffat, K. (2001) Time-resolved biochemical crystallography: a mechanistic perspective, *Chem. Rev. 101*, 1569−1581.
36. Schmidt, M., Ihee, H., Pahl, R., and Šrajer, V. (2005) Protein-ligand interaction probed by time-resolved crystallography, *Methods Mol. Biol. 305*, 115−154.
37. Bourgeois, D., Vallone, B., Schotte, F., Arcovito, A., Miele, A. E., Sciara, G., Wulff, M., Anfinrud, P., and Brunori, M. (2003) Complex landscape of protein structural dynamics unveiled by nanosecond Laue crystallography, *Proc. Natl. Acad. Sci. U.S.A. 100*, 8704−8709.
38. Schotte, F., Lim, M., Jackson, T. A., Smirnov, A. V., Soman, J., Olson, J. S., Phillips, G. N., Jr., Wulff, M., and Anfinrud, P. A. (2003) Watching a protein as it functions with 150-ps time-resolved x-ray crystallography, *Science 300*, 1944−1947.
39. Schotte, F., Soman, J., Olson, J. S., Wulff, M., and Anfinrud, P. A. (2004) Picosecond time-resolved X-ray crystallography: probing protein function in real time, *J. Struct. Biol. 147*, 235−246.
40. Šrajer, V., Ren, Z., Teng, T. Y., Schmidt, M., Ursby, T., Bourgeois, D., Pradervand, C., Schildkamp, W., Wulff, M., and Moffat, K. (2001) Protein conformational relaxation and ligand migration in myoglobin: a nanosecond to millisecond molecular movie from time-resolved Laue X-ray diffraction, *Biochemistry 40*, 13802−13815.
41. Šrajer, V., Teng, T., Ursby, T., Pradervand, C., Ren, Z., Adachi, S., Schildkamp, W., Bourgeois, D., Wulff, M., and Moffat, K. (1996) Photolysis of the carbon monoxide complex of myoglobin: nanosecond time-resolved crystallography, *Science 274*, 1726−1729.
42. Schmidt, M., Nienhaus, K., Pahl, R., Krasselt, A., Anderson, S., Parak, F., Nienhaus, G. U., and Šrajer, V. (2005) Ligand migration pathway and protein dynamics in myoglobin: a time-resolved

crystallographic study on L29W MbCO, *Proc. Natl. Acad. Sci. U.S.A. 102*, 11704−11709.
43. Bourgeois, D., Vallone, B., Arcovito, A., Sciara, G., Schotte, F., Anfinrud, P. A., and Brunori, M. (2006) Extended subnanosecond structural dynamics of myoglobin revealed by Laue crystallography, *Proc. Natl. Acad. Sci. U.S.A. 103*, 4924−4929.
44. Knapp, J. E., and Royer, W. E., Jr. (2003) Ligand-linked structural transitions in crystals of a cooperative dimeric hemoglobin, *Biochemistry 42*, 4640−4647.
45. Ren, Z., Perman, B., Šrajer, V., Teng, T. Y., Pradervand, C., Bourgeois, D., Schotte, F., Ursby, T., Kort, R., Wulff, M., and Moffat, K. (2001) A molecular movie at 18 Å resolution displays the photocycle of photoactive yellow protein, a eubacterial blue-light receptor, from nanoseconds to seconds, *Biochemistry 40*, 13788−13801.
46. Ihee, H., Rajagopal, S., Šrajer, V., Pahl, R., Anderson, S., Schmidt, M., Schotte, F., Anfinrud, P. A., Wulff, M., and Moffat, K. (2005) Visualizing reaction pathways in photoactive yellow protein from nanoseconds to seconds, *Proc. Natl. Acad. Sci. U.S.A. 102*, 7145−7150.
47. Baxter, R. H., Ponomarenko, N., Šrajer, V., Pahl, R., Moffat, K., and Norris, J. R. (2004) Time-resolved crystallographic studies of light-induced structural changes in the photosynthetic reaction center, *Proc. Natl. Acad. Sci. U.S.A. 101*, 5982−5987.
48. Schmidt, M., Rajagopal, S., Ren, Z., and Moffat, K. (2003) Application of singular value decomposition to the analysis of time-resolved macromolecular x-ray data, *Biophys. J. 84*, 2112−2129.
49. Rajagopal, S., Schmidt, M., Anderson, S., Ihee, H., and Moffat, K. (2004) Analysis of experimental time-resolved crystallographic data by singular value decomposition, *Acta Crystallogr., Sect. D: Biol. Crystallogr. 60*, 860−871.
50. Šrajer, V., Crosson, S., Schmidt, M., Key, J., Schotte, F., Anderson, S., Perman, B., Ren, Z., Teng, T. Y., Bourgeois, D., Wulff, M., and Moffat, K. (2000) Extraction of accurate structure-factor amplitudes from Laue data: wavelength normalization with wiggler and undulator X-ray sources, *J. Synchrotron Radiat. 7*, 236−244.
51. Ren, Z., Bourgeois, D., Helliwell, J. R., Moffat, K., Šrajer, V., and Stoddard, B. L. (1999) Laue crystallography: coming of age, *J. Synchrotron Radiat. 6*, 891−917.
52. Ursby, T., and Bourgeois, D. (1997) Improved Estimation of Structure-Factor Difference Amplitudesfrom Poorly Accurate Data, *Acta Crystallogr., Sect. A 53*, 564−575.
53. Gilles-Gonzalez, M. A., Gonzalez, G., Perutz, M. F., Kiger, L., Marden, M. C., and Poyart, C. (1994) Heme-based sensors, exemplified by the kinase FixL, are a new class of heme protein with distinctive ligand binding and autoxidation, *Biochemistry 33*, 8067−8073.
54. Ren, Z. (2004) *Precognition Users Guide*, RenZ Research, Inc.
55. (1994) The CCP4 Suite: Programs for Protein Crystallography, *Acta Crystallogr., Sect. D: Biol. Crystallogr. 50*, 760−763.
56. Carson, M. (1997) Ribbons, *Methods Enzymol. 277*, 493−505.
57. DeLano, W. L. (2002) The PyMOL Molecular Graphics System; DeLano Scientific, Palo Alto, CA.
58. Henry, E. R., and Hofrichter, J. (1992) Singular Value Decomposition −Application to Analysis of Experimental Data, *Methods Enzymol. 210*, 129−192.
59. Kleywegt, G. J., and Jones, T. A. (1994) Detection, delineation, measurement and display of cavities in macromolecular structures, *Acta Crystallogr., Sect. D: Biol. Crystallogr. 50*, 178−85.
60. Chen, Y., Šrajer, V., Ng, K., Legrand, A., and Moffat, K. (1994) Optical Monitoring of Protein Crystals in Time-Resolved X-Ray Experiments−Microspectrophotometer Design and Performance, *Rev. Sci. Instrum. 65*, 1506−1511.
61. Morikis, D., Sage, J. T., Rizos, A. K., and Champion, P. M. (1988) Resonance Raman studies of myoglobin single crystals, *J. Am. Chem. Soc. 110*, 6341−6342.
62. Liebl, U., Bouzhir-Sima, L., Negrerie, M., Martin, J. L., and Vos, M. H. (2002) Ultrafast ligand rebinding in the heme domain of the oxygen sensors FixL and Dos: general regulatory implications for heme-based sensors, *Proc. Natl. Acad. Sci. U.S.A. 99*, 12771−12776.
63. Rodgers, K. R., and Lukat-Rodgers, G. S. (2005) Insights into heme-based O2 sensing from structure-function relationships in the FixL proteins, *J. Inorg. Biochem. 99*, 963−77.
64. Key, J. (2004) Ph.D. Thesis, Department of Biochemistry Molecular Biology, The University of Chicago, Chicago, IL, p 186.
65. Brunori, M., Bourgeois, D., and Vallone, B. (2004) The structural dynamics of myoglobin, *J. Struct. Biol. 147*, 223−234.
66. Jasaitis, A., Hola, K., Bouzhir-Sima, L., Lambry, J. C., Balland, V., Vos, M. H., and Liebl, U. (2006) Role of distal arginine in early sensing intermediates in the heme domain of the oxygen sensor FixL, *Biochemistry 45*, 6018−6026.
67. Tilton, R. F., Jr., Kuntz, I. D., Jr., and Petsko, G. A. (1984) Cavities in proteins: structure of a metmyoglobin-xenon complex solved to 19 Å, *Biochemistry 23*, 2849−2857.
68. Schlichting, I., Berendzen, J., Phillips, G. N., Jr., and Sweet, R. M. (1994) Crystal structure of photolysed carbonmonoxy-myoglobin, *Nature 371*, 808−812.
69. Teng, T. Y., Šrajer, V., and Moffat, K. (1994) Photolysis-induced structural changes in single crystals of carbonmonoxy myoglobin at 40 K, *Nat. Struct. Biol. 1*, 701−705.
70. Teng, T. Y., Šrajer, V., and Moffat, K. (1997) Initial trajectory of carbon monoxide after photodissociation from myoglobin at cryogenic temperatures, *Biochemistry 36*, 12087−12100.
71. Hartmann, H., Zinser, S., Komninos, P., Schneider, R. T., Nienhaus, G. U., and Parak, F. (1996) X-ray structure determination of a metastable state of carbonmonoxy myoglobin after photodissociation, *Proc. Natl. Acad. Sci. U.S.A. 93*, 7013−6.

BI700043C